Constructing function domains in NiTi shape memory alloys by additive manufacturing

H. Z. Lu, T. Chen, L. H. Liu, H. Wang, X. Luo, C. H. Song, Z. Wang & C. Yang

Taylor & Francis
Taylor & Francis Group

Check for updates

Constructing function domains in NiTi shape memory alloys by additive manufacturing

H. Z. Lu[a], T. Chen[a], L. H. Liu[a], H. Wang[b], X. Luo[a], C. H. Song[a], Z. Wang[a] and C. Yang[a]

[a]National Engineering Research Center of Near-net-shape Forming for Metallic Materials, Guangdong Provincial Key Laboratory for Processing and Forming of Advanced Metallic Materials, South China University of Technology, Guangzhou, People's Republic of China; [b]College of Mechatronics and Control Engineering, Shenzhen University, Shenzhen, People's Republic of China

ABSTRACT

Additive manufacturing (AM) is an orderly construction process involving track-by-track melt pools, which can modulate three characteristic zones between two adjacent melt pools: the heat-affected zone, transition zone, and cellular grain zone. These three zones constitute a function domain that determines the properties of AM metallic materials. In this study, we constructed a novel ordered function domain by AM of modified $Ni_{50.6}Ti_{49.4}$ shape memory alloy powder, which was produced by adding uniform Ni nanoparticles into atomised $Ni_{49.6}Ti_{50.4}$ powder. Interestingly, the three zones of the function domain had the same B2 austenite matrix but inhomogeneous Ni_4Ti_3 clusters and Ti_2Ni nanoprecipitates, which caused different compressive recovery and residual strains in the three zones. The synergetic effect of the three zones generated a stable recovery strain and small hysteresis area in the AMed $Ni_{50.6}Ti_{49.4}$. Our results provide a novel strategy for modulating the microstructure of NiTi by AM to yield superior properties.

Constructing function domains in NiTi SMAs by additive manufacturing
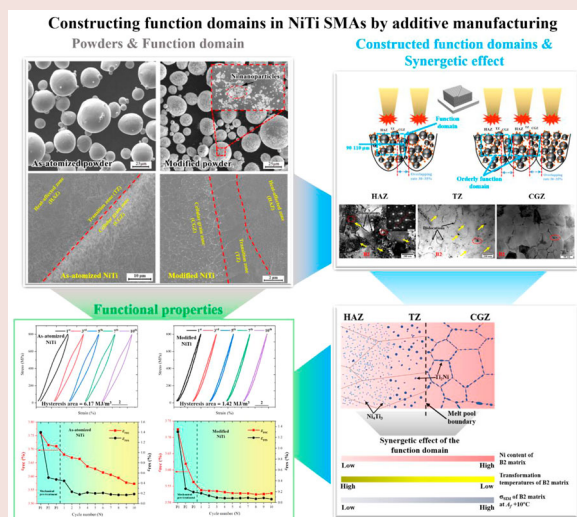
1. Introduction

Owing to their advantages of superelasticity, shape memory effect, good biocompatibility, and high corrosion resistance, NiTi shape memory alloys (SMAs) are widely used in aerospace applications, surgical instruments, and medical devices (Elahinia et al. 2012; Jani et al. 2014). The superelasticity of NiTi SMAs, which allows them to recover from large amounts of strain, originates from a diffusion-less phase transformation,

B2 austenite ↔ B19′ martensite, which is activated by mechanical stress under isothermal conditions. Extensive research has confirmed that the grain size and precipitate phases are two parameters that control the critical stress (σ_{SIM}) for the stress-induced transformation B2 → B19′ in NiTi SMAs, thereby affecting dislocation formation (Otsuka and Ren 2005). (Khalil-Allafi, Dlouhy, and Eggeler 2002; Lu et al. 2021) confirmed that two types of precipitates, Ni_4Ti_3 and Ti_2Ni, play important roles in tailoring the superelasticity of NiTi SMAs. The lattice

mismatch between the Ni_4Ti_3 precipitates and B2 austenite matrix causes internal stress around the precipitates, which can alter the $B2 \leftrightarrow B19'$ phase-transformation temperature. Furthermore, (Chen et al. 2019) reported that Ni_4Ti_3 precipitates with a specific size can generate precipitation hardening, resulting in a higher critical stress for dislocation slip or a higher yield strength for the B2 matrix. For instance, 40–70 nm Ni_4Ti_3 precipitates can induce enhanced compressive superelasticity (recovery strain of 4.6%) in $Ni_{51.4}Ti_{48.6}$ SMAs produced by laser powder-bed-fusion additive manufacturing (AM) and aging, as elaborated by (Cao et al. 2020). In addition, (Hou et al. 2019; Chu and Sun 2021) indicated that the decrease in the hysteresis area in the stress–strain curves caused by superelasticity can be attributed to the formation of saturated dislocations and residual nanoscale $B19'$ martensite in $Ni_{50.8}Ti_{49.2}$ SMAs or the formation of a non-transformable phase in the B2 matrix of $Ni_{51.5}Ti_{48.5}$ SMAs fabricated by laser directed energy deposition.

In the case of Ti_2Ni precipitates, their relatively small size and semi-coherent interface with the B2 matrix can induce precipitation hardening and consequently enhance the yield strength of B2 austenite, as observed by (Tomozawa, Kim, and Miyazaki 2009; Lu et al. 2022). The formation of Ni_4Ti_3 and Ti_2Ni precipitates is dependent on the alloy composition and processing conditions, with Ni_4Ti_3 and Ti_2Ni preferentially precipitating in Ni-rich and Ti-rich NiTi SMAs, respectively (Otsuka and Ren 2005). However, owing to the unique characteristics of AM, Ti_2Ni or $Ti_4Ni_2O_x$ precipitates can form in equiatomic $Ni_{50}Ti_{50}$ and Ni-rich $Ni_{50.6}Ti_{49.4}$ SMAs (Zhang, Chen, and Coddet 2013; Gu et al. 2021a). Furthermore, both Ni_4Ti_3 and Ti_2Ni precipitates can form simultaneously in Ni-rich $Ni_{51.3}Ti_{48.7}$ SMAs fabricated by selective electron beam melting and $Ni_{50.9}Ti_{49.1}$ SMAs fabricated by laser powder bed fusion owing to non-equilibrium rapid solidification and a complex thermal history (Franco et al. 2017; Zhou et al. 2019). Therefore, the formation mechanisms of these precipitate phases in AM NiTi SMAs should be investigated to determine whether they differ and their effect on the functional properties of NiTi SMAs.

AM can revolutionise the manufacturing of three-dimensional metallic parts by the integration of design flexibility and the rapid fabrication of complex parts through the bottom-up accumulation of powder material (Gu et al. 2021b; Zhang and Liu 2022). For NiTi SMAs, post-machining is very challenging because of the low thermal conductivity of intermetallic compounds, high work hardening, and remarkable spring back effect, as stated by (Elahinia et al. 2016). To minimise the need for post-machining, numerous efforts have been made to fabricate NiTi SMAs by AM to expand their applications (Lu et al. 2019; Alagha, Hussain, and Zaki 2021). Physically, AM is an orderly construction process in which solid powder particles are rapidly melted and subsequently solidified track-by-track and layer-by-layer. These ordered melt pools and the associated cyclic thermal history generally result in three characteristic zones between two adjacent melt pools: the heat-affected zone (HAZ), transition zone (TZ), and cellular grain zone (CGZ) (Kou 2002; Oliveira, Miranda, and Braz Fernandes 2017). These three zones constitute an elementary domain, which is hereafter referred to as the function domain. To date, the microstructure of these characteristic zones and their influence on the functional properties of AM NiTi SMAs have not been revealed in detail.

Given the complex thermal history inside a function domain in AM NiTi SMAs and the different precipitation kinetics of Ni_4Ti_3 and Ti_2Ni precipitates, it can be hypothesised that these two precipitates will form in different locations. This theory is supported by the preferential formation of Ni_4Ti_3 precipitates in the HAZ of the function domain in laser-processed $Ni_{50.8}Ti_{49.2}$ SMAs, as observed by (Oliveira et al. 2018). Unfortunately, the specific precipitation locations of Ni_4Ti_3 and Ti_2Ni and their effect on the functional properties of AMed NiTi SMAs are not clear, although the two types of precipitates can form simultaneously (Franco et al. 2017; Sam et al. 2018; Zhou et al. 2019). In addition, the physical properties of NiTi SMAs are very sensitive to the Ni/Ti atomic ratio. (Frenzel et al. 2010) found that even a slight variation of 0.1 at.% can significantly affect the $B2 \leftrightarrow B19'$ transformation temperature by as much as 10~20°C. Hypothetically, this effect can be attributed to the different thermal histories and Ni_4Ti_3 and Ti_2Ni precipitation behaviours inside the characteristic zones in the function domain. This discussion gives rise to the following question: *Can AM be used to modulate and direct the construction of the function domain to include different precipitates in different characteristic zones to control the physical properties of NiTi SMAs?*

In this study, we report the orderly construction of the function domain in a $Ni_{50.6}Ti_{49.4}$ SMA during AM using a laser powder bed fusion process. Interestingly, the results show that the function domain in the AM SMA consists of three ordered characteristic zones (HAZ, TZ, and CGZ) with different grain sizes and an inhomogeneous distribution of Ni_4Ti_3 and Ti_2Ni precipitates. As a result, the synergetic effect in the three characteristic zones results in a stable recovery strain and a small hysteresis area in the AM SMA. We believe that the results obtained herein will provide a novel strategy to tailor the microstructure of NiTi SMAs via AM to achieve superior physical properties.

2. Experimental

As-atomised $Ni_{49.4}Ti_{50.6}$ (nominal composition in atomic ratio) was prepared by electrode induction melting gas atomisation (AMC Powders Co., Ltd., Beijing). To control the Ni content and obtain a modified $Ni_{50.6}Ti_{49.4}$ powder, high-purity elemental Ni nanoparticles (100 nm, 99.9 wt.%) were added to the as-atomised $Ni_{49.4}Ti_{50.6}$ powder in a protective Ar atmosphere in a glove box; the mass ratio of Ni nanoparticles and as-atomised $Ni_{49.4}Ti_{50.6}$ powder was calculated to be 1:37. Subsequently, low-energy ball milling was conducted at $1 s^{-1}$ for 60 min in a protective Ar atmosphere to modify, mix, and homogenise the Ni nanoparticles with the as-atomised powder. The choice of Ni-rich $Ni_{50.6}Ti_{49.4}$ modified composition was based on two factors. Firstly, the Ni-rich (Ni > 50 at.%) modified SMA was designed to fabricate NiTi with superelastic properties. Secondly, this relatively high Ni composition (50.6 at.%) in modified powder provided a compositional condition for the formation of a large number of Ni_4Ti_3 precipitates in NiTi, which were effective to enhance superelastic properties of NiTi. The particle-size distribution, oxygen content, and zeta potential were characterised using a HORIBA laser scattering analyzer (LA960S, Japan), TC600 Nitrogen/Oxygen Determinator (LECO Co., USA), and Zetasizer Nano ZS (Malvern Panalytical Co., UK) with water as the dispersant, respectively. To evaluate the laser absorptivity, the modified and as-atomised powders were placed in quartz cuvettes, sealed, and analyzed by diffuse reflectance spectroscopy in the wavelength range 400–2250 nm using a UV–visible–near-infrared (NIR) spectrophotometer (Lambda 900, PerkinElmer, USA).

NiTi SMAs based on the two powders (as-atomised and modified powders) were additively manufactured using a laser powder bed fusion system (Concept Laser M2 Cusing) in a protective Ar atmosphere. The processing parameters were a laser power of 70 W, laser scanning speed of 105 mm/s, powder layer thickness of 30 μm, hatch spacing of 100 μm, and laser track overlap rate of 30% to 35% based on the optimisation performed in our previous study (Lu et al. 2019). In this work, an alternating angle of ±45° (with respect to the x-axis) between consecutive layers was used as the laser scan path. It should be noted that the detailed effect of altered scan path on the construction of ordered structures is needed to be investigated in future work. The dimensions of the AM SMAs were $10 \times 10 \times 10$ mm (Figure 1). The phase components and transformation temperatures of the AM SMAs were examined by XRD (D/MAX-2500/PC) with Cu Kα radiation and DSC (Netzsch 204F1) at heating/cooling rates of 10°C/min in an Ar atmosphere, respectively. To

reveal the microstructural evolution, the AM SMAs were sampled, polished, etched, and observed by optical microscopy (Leica DM 15000M) and field-emission SEM (A Philips XL-30 FEG) coupled with EDS. For electron backscatter diffraction (EBSD) analysis, the AM SMAs were immersed in an electrolyte composed of 80 vol.% ethanol and 20 vol.% sulfuric acid and treated on an electrolytic polishing device (EP-06, Shanghai). EBSD tests were conducted using SEM, and the obtained data were post-processed using the HKL-Channel 5 software. Field-emission HRTEM (Tecnai G2 F30, USA) was used to study the microstructure of the AM SMAs, particularly the Ni_4Ti_3 and Ti_2Ni precipitation behaviours in the function domain. In addition, Image Pro-Plus software was used to measure the size of precipitates, and at least 100 precipitates were measured to determine their mean grain size.

To evaluate the Young's modulus and nanohardness of the three characteristic zones, nanoindentation tests were performed using a high-precision nanohardness tester (TTX-NHT3, Anton Paar, Austria) with a test force of 5000 μN. For thermomechanical analysis, ⌀3 × 6 mm samples were cut perpendicular to the AM building direction and subjected to stress-controlled cyclic compressive loading on an Instron 8862 test platform equipped with a precise extensometer. The samples were heated to 10°C above the austenite transformation finish temperature (A_f) and held for 5 min to ensure temperature uniformity before conducting the thermomechanical tests. Subsequently, a load of 800 MPa was applied, which was later unloaded to 10 MPa. The loading and unloading processes were cycled 10 times at a strain rate of $5 \times 10^{-4} s^{-1}$.

To clarify the formation mechanism of the Ni_4Ti_3 and Ti_2Ni precipitates in the three ordered characteristic zones in the function domain, FLOW-3D software was used to conduct numerical simulations of the AM process. A finite-element method based on mesoscale models was employed to describe the evolution of the thermal histories in the melt pools formed by two adjacent laser tracks (Lee and Zhang 2016). A structured Eulerian mesh with a cell size of 4 μm was used for these simulations. These number simulations are based on the conservation laws of fluid dynamics, discretized in a regular 3D spatial array in Cartesian coordinates; meanwhile, the complicated physical processes such as melting, phase change, and melt pool flow were numerically solved by computational fluid dynamics. The molten metal was assumed to be Newtonian and incompressible. The model numerically solved the conservation equations of mass, momentum and energy, which are given by (Lee and Zhang 2016). Because both the as-atomised and modified powders had near-
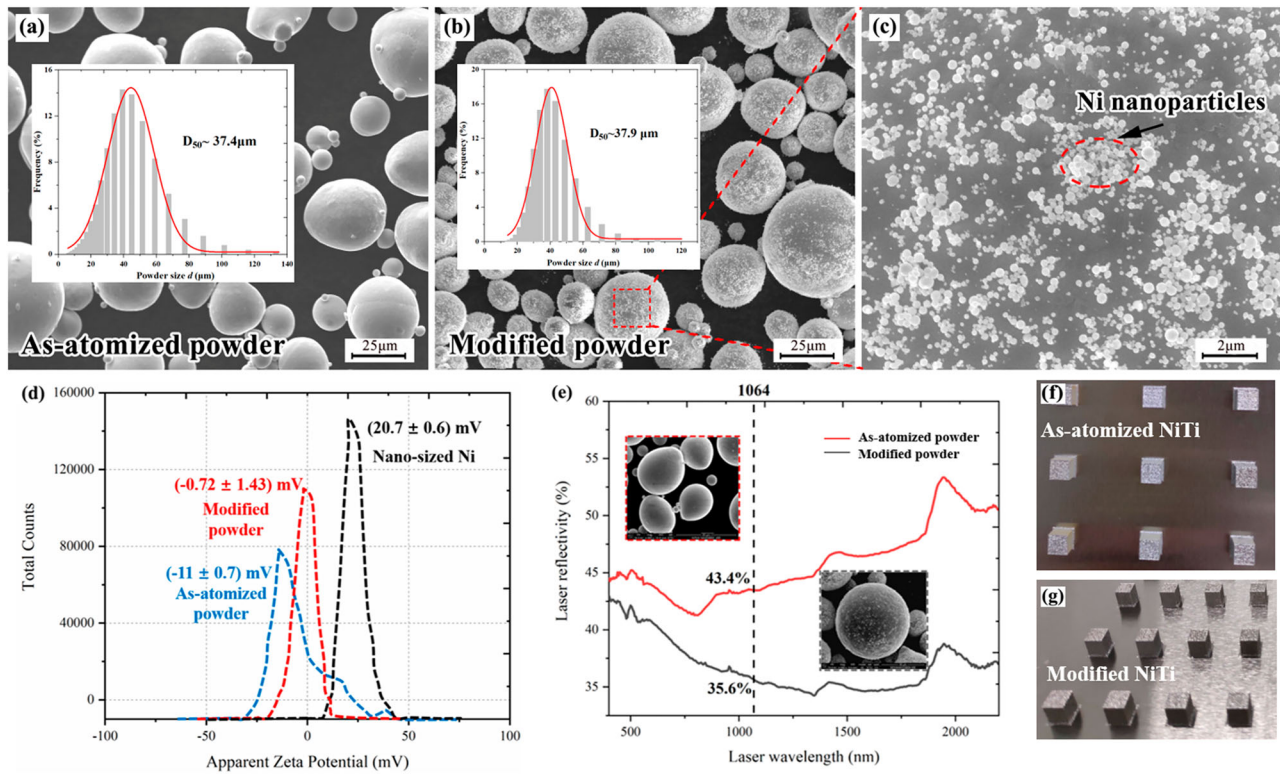
Figure 1. (a–c) SEM images and particle-size distributions (insets in a and b) of the as-atomised and modified powders. (d) Zeta potential of the Ni nanoparticles, as-atomised powder, and modified powder. (e) Laser reflectivity of the as-atomised and modified powders. (f and g) AMed SMAs with $10 \times 10 \times 10$ mm.

equiatomic Ti and Ni contents, the thermophysical properties of a NiTi SMA were employed for numerical simulations, as presented in Table 1 (Brandes and Brook 1983; Committee 1990).

3. Results

3.1. Powders and AMed NiTi SMAs

Figure 1a–c shows scanning electron microscopy (SEM) images depicting the morphologies and particle-size distributions of the as-atomised and modified powders. The

Table 1. Thermophysical properties of NiTi SMAs used in numeral simulations.

Parameters	Symbol	Values (units)
Density	ρ	6 g·cm^{-3}
Viscosity	μ	5.05×10^{-3} Pa·s
Thermal conductivity	λ	18 W·m^{-1}·K^{-1}
Surface tension	γ_s	1.714 N·m^{-1}
Solidus temperature	T_S	1583 K
Liquidus (melting) temperature	T_L	1583 K
Boiling temperature	T_{LV}	3005 K
Specific heat	C_p	840 J·kg^{-1}·K^{-1}
Latent heat of vaporisation	ΔH_{LV}	378 kJ·mol^{-1}
Latent heat of fusion	L_f	2.57 kJ·mol^{-1}
Stefan-Boltzmann constant	σ_s	5.67×10^{-8} W·m^{-2}·K^{-4}
Convection coefficient	h_A	80 W·m^{-2}·K
Universal gas constant	R	8.3144 J·K^{-1}·mol^{-1}
Temperature of environment	T_∞	293 K

as-atomised powder contained spherical or near-spherical particles with a few small satellite particles (Figure 1a), and their median diameter (D_{50}) was 37.4 μm (Figure 1a inset). The modified powder also exhibited a spherical morphology with uniformly distributed Ni particles on the spherical surfaces (Figure 1b and c). It should be noted that the D_{50} of the modified powder was 37.9 μm, which is only 0.5 μm larger than that of the as-atomised powder (Figure 1b inset). This indicates that the difference between the sizes of the as-atomised and modified powders did not significantly affect the AM process. In addition, the oxygen contents of the as-atomised and modified powders were 650 and 1100 ppm, respectively.

Figure 1d shows zeta-potential curves of the Ni nanoparticles and the as-atomised and modified powders. The zeta potential is the potential difference between the surface of a solid particle immersed in a conducting liquid (e.g. water) and the conducting liquid; it is an indicator of the affinity between the two types of powders (Guo et al. 2018; Hossain et al. 2020). The zeta potentials of the Ni nanoparticles, as-atomised powder, and modified powder were 20.7 ± 0.6, -11 ± 0.7, and -0.72 ± 1.43 mV, respectively. This suggests that the Ni nanoparticles combined with and were coated on the surface of the as-atomised powder during the mixing

and homogenisation processes. Furthermore, this resulted in a uniform distribution of Ni nanoparticles on the surfaces of the modified powder (Figure 1b and c). Interestingly, the uniform distribution described here is different from the preferred agglomeration of nanoparticles, such as for 800 nm V_8C_7 particles added to 37.8 μm 316 L stainless-steel powder, as observed by (Li et al. 2019), 1–4 μm B_4C particles added to 35 μm Ti6Al4 V powder and subjected to high-energy ball milling, as observed by (Fereiduni, Ghasemi, and Elbestawi 2019), and 100–500 nm ZrH_2 particles added to 45 μm Al7075 powder by electrostatic assembly, as observed by (Martin et al. 2017). Therefore, the unique modification mechanism in this study ensured that the modified powder was suitable for fabricating bulk NiTi alloys by AM.

Figure 1e shows the variation in the laser reflectivity with laser wavelength of the as-atomised and modified powders. Generally, the processability of a powder is influenced by a variety of physical and chemical properties, including laser absorptivity, morphology, size, and surface states (Herzog et al. 2016). Specifically, laser absorptivity determines the amount of power a loosely piled powder can absorb at a given laser wavelength before forming a melt pool. This can be assessed by the associated laser reflectivity of the powder. As shown in Figure 1e, the laser reflectivity of the modified powder at 1064 nm was 35.6%, that is, it was 7.8% lower than that of the as-atomised powder. The smaller laser reflectivity of the modified powder implies that it exhibits improved laser absorptivity, which is expected to enhance the processability of the powder (Li et al. 2017).

Figure 2 shows surface morphologies, spot energy dispersive spectrometry (EDS) results, X-ray diffraction (XRD) patterns, and differential scanning calorimetry (DSC) thermograms of the different NiTi SMAs (as-atomised and modified NiTi). The excellent processability of the modified powder is evident by the absence of microcracks and holes and the smooth and stable laser tracks (Figure 2b). The modified powder had a slightly larger quantity of spatter powder than that of the as-atomised powder. It is expected that spatter powder would be more likely to form on the surface of the modified NiTi rather than on the as-atomised NiTi owing to the more intense reaction between the modified powder and the laser. EDS analysis (inset in Figure 2a and b) indicates that the Ni contents were 49.56 and 49.34 at.% in the spatter powder and laser track produced with the as-atomised powder, respectively, while they were 50.74 and 50.13 at.% in the spatter powder and laser track produced with the modified powder. This proves that the Ni nanoparticles were effective in tailoring the Ni/Ti atomic ratio.

According to the XRD results, the as-atomised NiTi was composed of B19′ martensite (major component), B2 austenite (minor component), and Ti_2Ni precipitates (Figure 2c). In contrast, the modified NiTi exhibited three strong diffraction peaks corresponding to the (110), (200), and (211) Miller indices of B2 austenite. This indicates that B2 austenite was the predominant component in the modified NiTi. Further XRD analysis revealed that Ni_4Ti_3 and Ti_2Ni precipitates were also present in the modified NiTi (Figure 2c). Differences in the phases and precipitates can lead to different thermal and physical properties in NiTi alloys. As shown in Figure 2d, although both the as-atomised and modified NiTi underwent B19′ → B2 and B2 → B19′ transformations during heating and cooling, respectively, they exhibited very different phase-transformation temperatures, including austenite start (A_s), austenite finish (A_f), martensite start (M_s), and martensite finish (M_f) temperatures. The A_s, A_f, M_s, and M_f values were 55.2, 81.7, 57.8, and 6.5°C, respectively, for as the as-atomised NiTi, and −42.8, 56.9, 11.7, and −56.7°C (Figure 2d), respectively, for the modified NiTi. In addition, the modified NiTi exhibited a wider A_f–A_s range (99.7°C), which was 73.2°C greater than that of the as-atomised NiTi. This is associated with the formation of different precipitates in the three ordered characteristic zones in the modified NiTi, which will be discussed in Section 4.2.

3.2. Microstructures of the three characteristic zones in the function domain

Figure 3 shows the microstructures of the as-atomised NiTi. No microcracks or pores were observed in the optical images (Figure 3a and b). Furthermore, laser tracks and melt-pool boundaries were formed at the top surface (Figure 3c) owing to the Gaussian energy distribution of the laser (Verhaeghe et al. 2009). High-magnification SEM images suggested the formation of the three characteristic zones (HAZ, TZ, and CGZ), and these zones were separated by melt-pool boundaries (Figure 3c). Figure 3d–f present SEM images of the three zones, in which Ti_2Ni nanoprecipitates are marked by yellow arrows. Based on statistical analysis using ImageJ software, the CGZ occupied approximately 30% of the function domain. Further transmission electron microscopy (TEM) results (Figure 3g–i) showed that B19′ martensite was the major matrix phase in the as-atomised NiTi, consistent with the XRD results in Figure 2c. It should be noted that TEM-EDS results of these nanoprecipitates (not shown here) confirmed the composition of these precipitates as Ti_2Ni phase. Although the three zones had the same Ti_2Ni
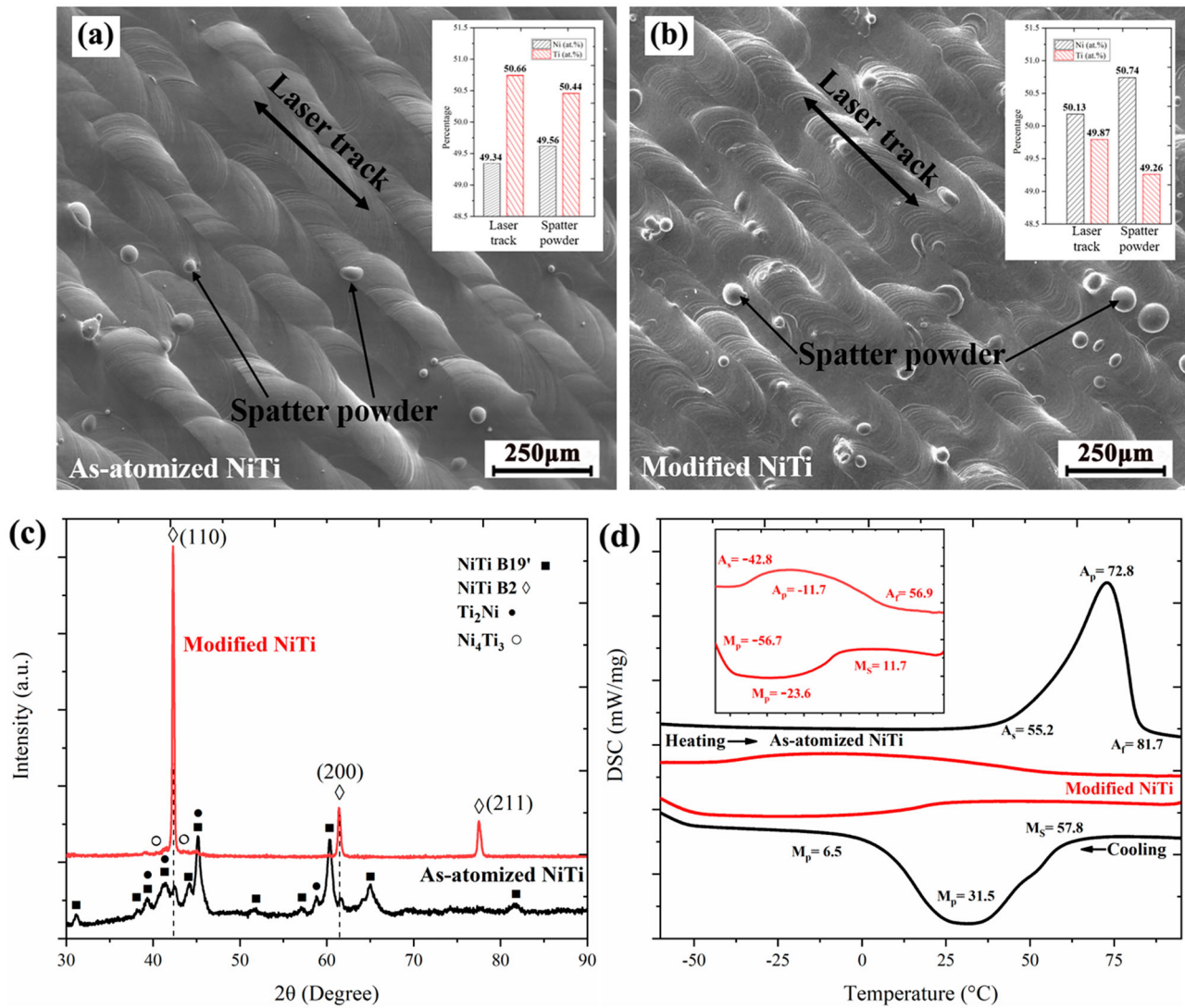
Figure 2. (a, b) SEM images and EDS analysis, (c) XRD patterns, and (d) DSC scans of the as-atomised and modified NiTi.

nanoprecipitates (marked by yellow arrows and similar to those in $Ni_{50.9}Ti_{49.1}$ and $Ni_{49.4}Ti_{50.6}$ SMAs fabricated by laser powder bed fusion AM [Franco et al. 2017; Lu et al. 2019]), the precipitates had different sizes and formed in different locations. Specifically, the Ti_2Ni nano-precipitates were distributed homogeneously in the matrix of the HAZ and TZ and semi-continuously along the grain boundaries of the CGZ. The diameters of the precipitates in the HAZ, TZ, and CGZ were approximately 50, 60, and 45 nm, respectively. The difference in the location of the Ti_2Ni precipitates is attributed to the different thermal histories in different zones in the function domain, which will be discussed in Section 4.1.

Figure 4 shows the microstructures of the modified NiTi. Similar to the as-atomised NiTi (Figure 3), the modified NiTi did not contain visible microcracks and pores (Figure 4a), had laser tracks separated by melt-pool boundaries (Figure 4b), and exhibited the three

ordered characteristic zones (HAZ, TZ, and CGZ) in the function domain (Figure 4c). The CGZ in the modified NiTi occupied approximately 18% of the function domain, 12% less than that in the as-atomised NiTi. In general, the three characteristic zones in Figures 3 and 4 were associated with the function domain orderly con-structed during AM. This scenario was similar to those observed in AM and welded NiTi alloys (Oliveira, Miranda, and Braz Fernandes 2017). EBSD results revealed that the average grain sizes of the modified NiTi at top and side surface were 4.4 and 7.6 μm, respect-ively (Figure 4e and f). Some fine B2 grains with different orientations were distributed along the grain boundaries of large B2 grains (Figure 4d and e). Furthermore, EBSD analysis indicated that a weak texture along the [001] direction formed in the modified NiTi (Figure 4e and f) owing to the high temperature gradient parallel to the building direction, which could promote the directional
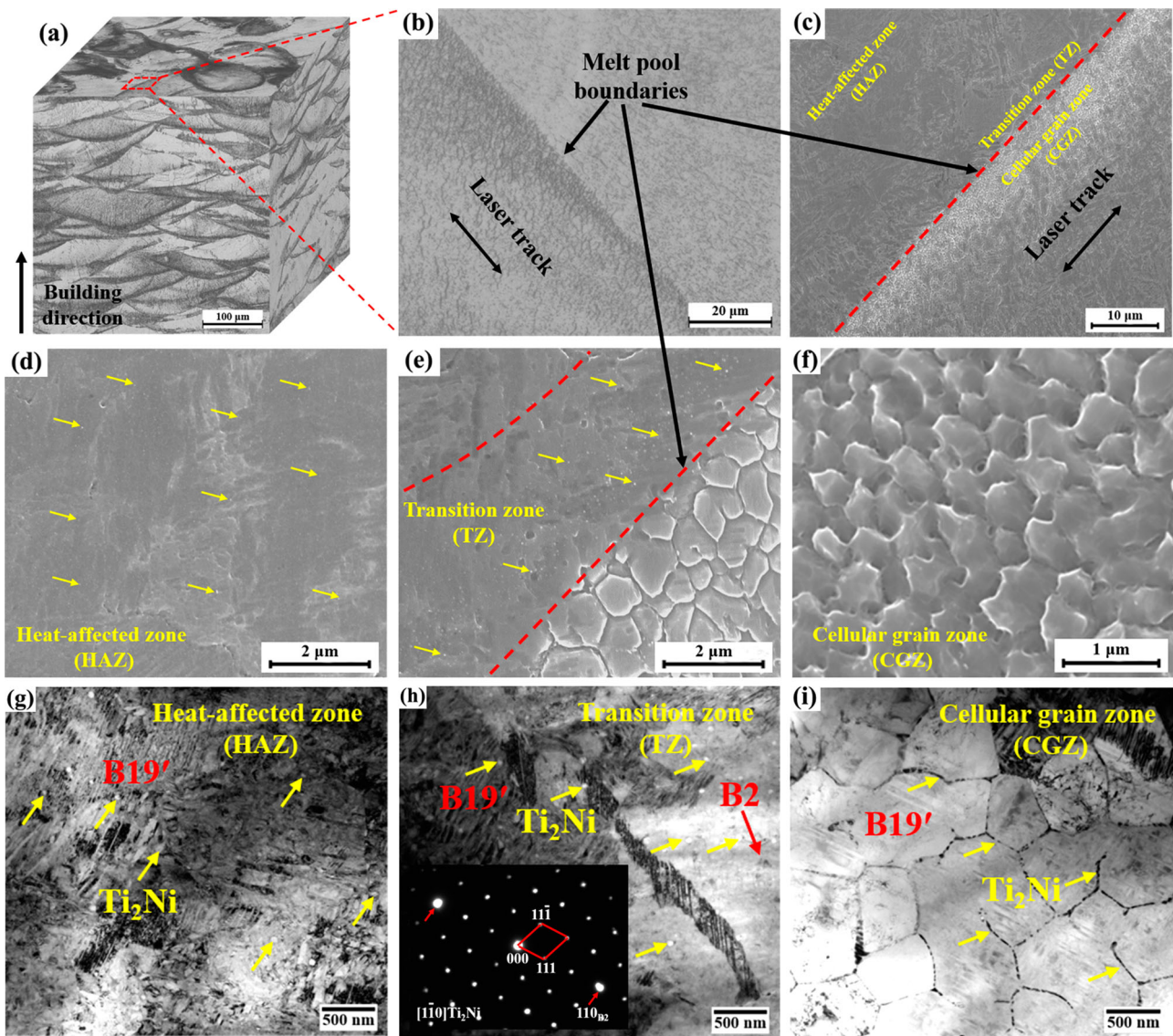
Figure 3. Microstructures of the as-atomised NiTi. (a) Three-dimensional optical image, (b) optical image of the top surface highlighted in (a), (c) SEM image of the three characteristic zones in the function domain, and (d–f) SEM images and (g–i) bright-field TEM images of the three characteristic zones.

growth of grains. However, the intensity of the texture along the [001] direction at top and side surface were only 1.79 and 3.20, which are considerably smaller than the strong texture along the [001] direction (18.2) in $Ni_{50.8}Ti_{49.2}$ SMAs fabricated by laser powder bed fusion AM, as observed by (Moghaddam et al. 2019). EBSD results with a high resolution for as-atomised NiTi can not be obtained owing to its extremely fine size of the B19′ martensite plates (a few tens of nanometers, Figure 3g–i), which is out of the ability of the EBSD instrument to catch clear Kikuchi patterns. Thus, no EBSD results for as-atomised NiTi was shown. Figure 4g shows schematics of microstructural formation in the modified NiTi. During the orderly construction of melt pools, the modified NiTi with uniformly distributed Ni

nanoparticles in layer N + 1 would be instantaneously melted under the laser beam. Then, the melted Ni nanoparticles in local areas of layer N + 1 could provide instantaneous concentration fluctuations, thus promoting the nucleation of B2 grains (red arrows in Figure 4g) and the formation of fine B2 grains (Figure 4d and e) (Martin et al. 2017). This would hinder epitaxial growth of columnar grains along the [001] direction in layer N (Lu et al. 2020), thereby causing a considerably weaker texture along the [001] direction (Figure 4e and f). Subsequently, the Ni atoms in the melted Ni nanoparticles would diffuse into the melted $Ni_{49.4}Ti_{50.6}$ liquid particles to achieve a uniform elemental distribution in the $Ni_{50.6}Ti_{49.4}$ liquid in layer N + 1. Next, the associated microstructures and functional properties of the orderly constructed melt
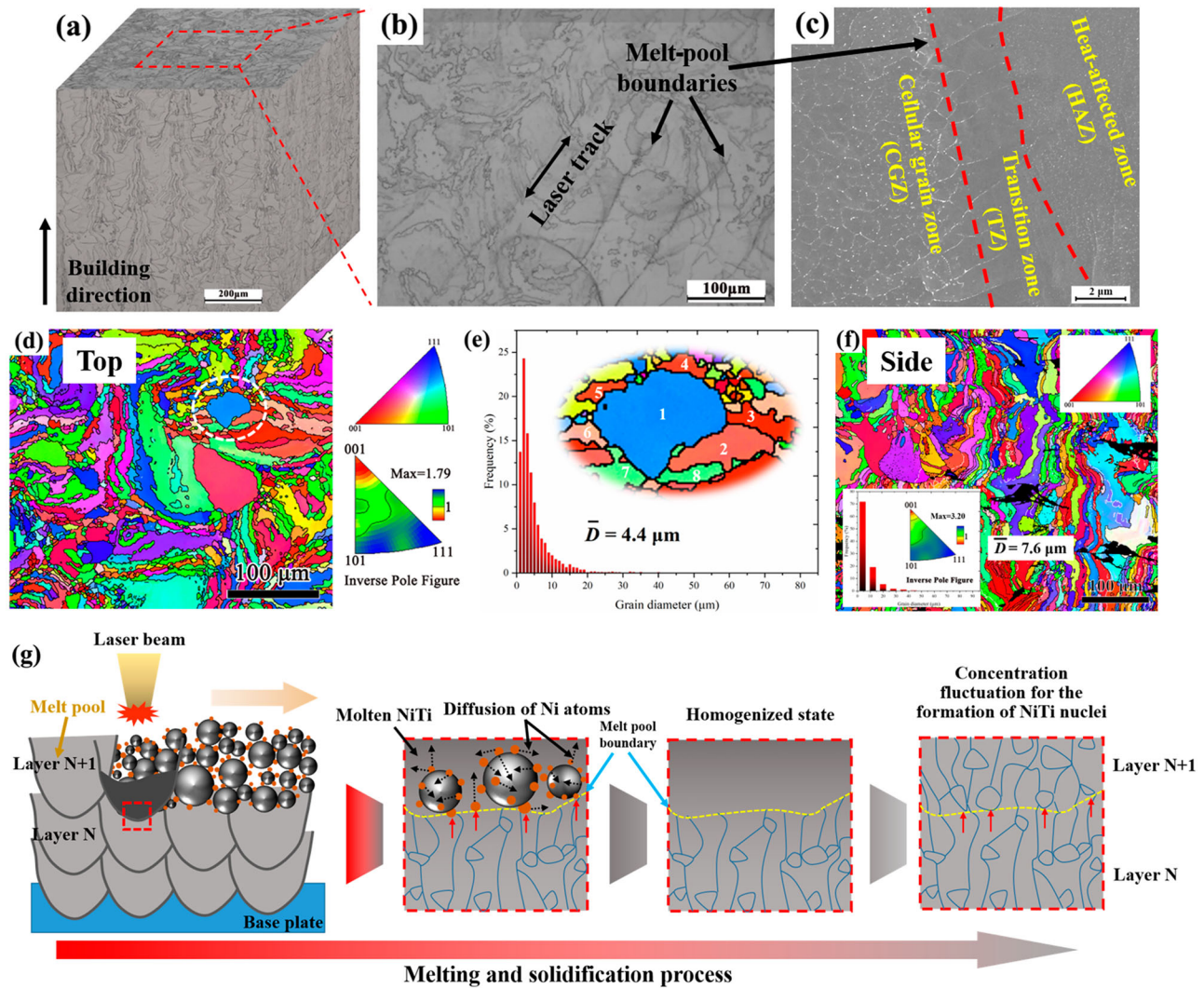
Figure 4. Microstructures of the modified NiTi. (a) Three-dimensional optical image, (b) optical image of the top surface highlighted in (a), (c) SEM image of the three characteristic zones in the function domain, (d) EBSD crystal orientation–color relation map and inverse pole figure corresponding to the top view, (e) grain-size distribution corresponding to the EBSD map, (f) EBSD results and inverse pole figure corresponding to the side view, and (g) schematics of microstructural formation resulting in weak texture along the [001] direction in the modified NiTi.

pool or the function domain and their underlying mechanisms will be discussed in detail.

Figure 5 presents SEM images and EDS maps of the three characteristic zones in the as-atomised and modified NiTi. For both NiTi SMAs, Ni and Ti were almost uniformly distributed inside the three characteristic zones, and there was no pronounced elemental segregation at the micrometer scale, which was consistent with prior work by (Cao et al. 2020). The results of EDS mapping demonstrated that all Ni nanoparticles had been melted and diffused homogeneously during laser powder bed fusion process. Simultaneously, it should be noted that the elements in the matrix would be altered owing to formation of different precipitate phases in the three zones in the function domain, which will be discussed in Section 4.2.

Figure 6 shows bright-field TEM images of the three characteristic zones in the function domain of the modified NiTi. Correspondingly, Figure 7 presents TEM-EDS results of different nanoprecipitates observed different regions (I, II, III, and IV) in Figure 6. At least five different nanoprecipitates at three characteristic zones were tested by TEM-EDS to get the element concentration, and the average values were presented by the inserts table in Figure 7. High-density dislocations can be distinctly observed inside the B2 austenite matrix in the HAZ and TZ (Figure 6a and b). Interestingly, compared with those in the as-atomised NiTi, the precipitates in the three zones in the function domain of the modified NiTi had the same precipitation locations but different phase types and smaller grain sizes. An abundant number of lath clusters formed inside the B2
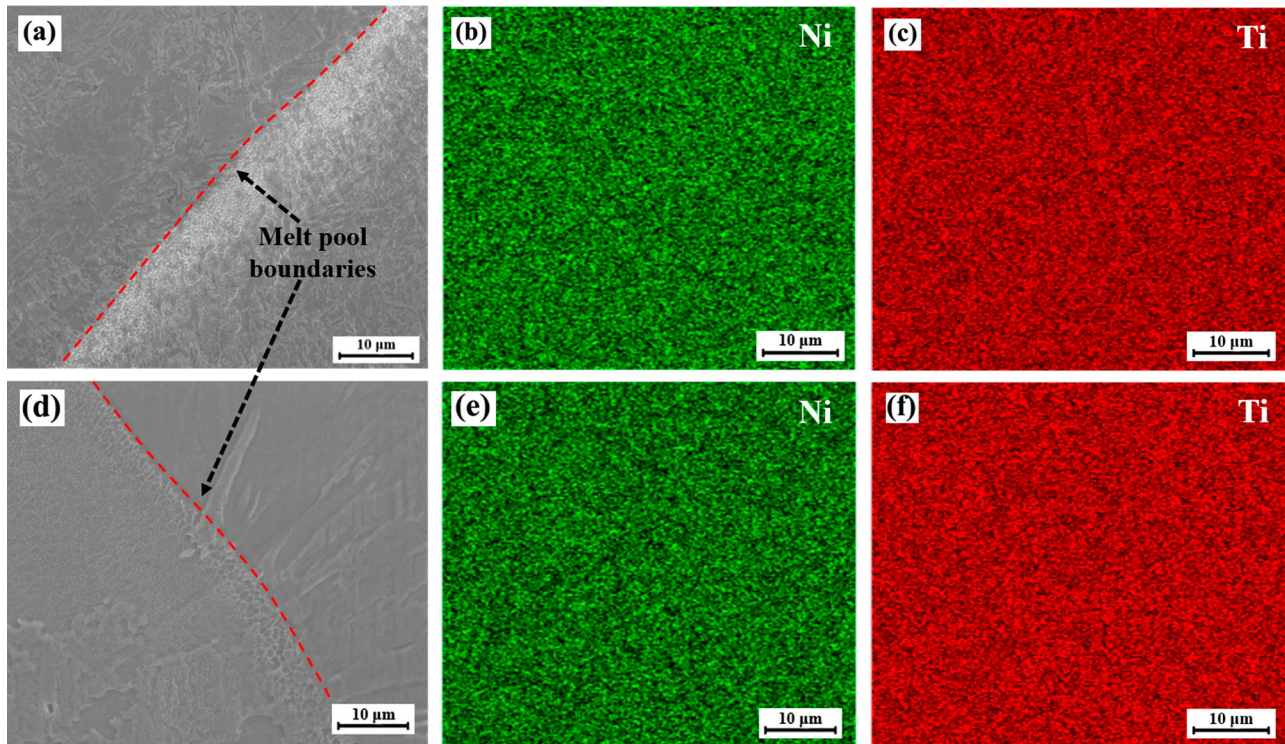
Figure 5. (a, d) SEM images and (b, c, e, f) EDS maps of the three characteristic zones in the as-atomised (a–c) and modified (d–f) NiTi.

austenite matrix of the HAZ, as marked by the yellow arrows in Figure 6a. The corresponding selected area electron diffraction (SAED) patterns (Figure 6a inset) were located at 1/7 positions along the <123> reciprocal vectors of the B2 austenite matrix, thus confirming the formation of Ni_4Ti_3 lath clusters (Otsuka and Ren 2005).
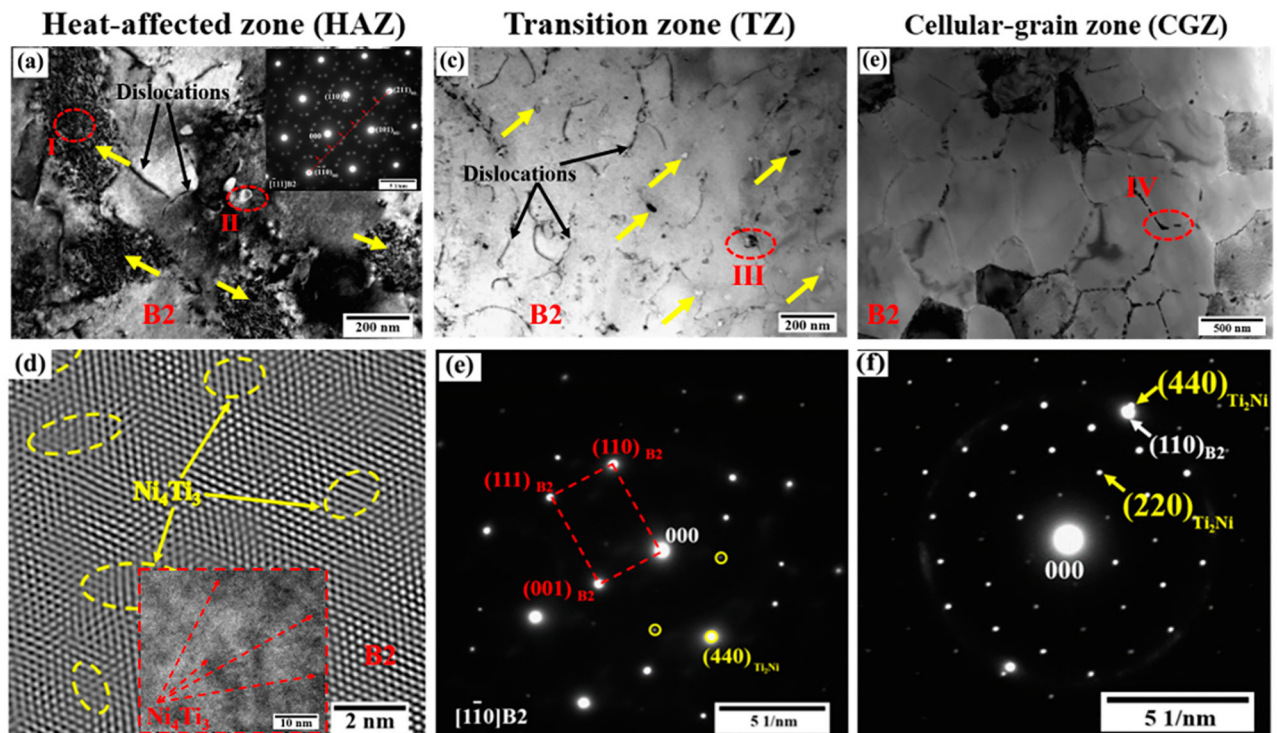

Figure 6. Bright-field TEM images of the modified NiTi. (a) HAZ, (b) TZ, (c) CGZ, (d) IFFT image of the red dotted circle (I) in (a), and (e, f) SAED patterns of the red dotted circles (III and IV) in (b) and (c), respectively.
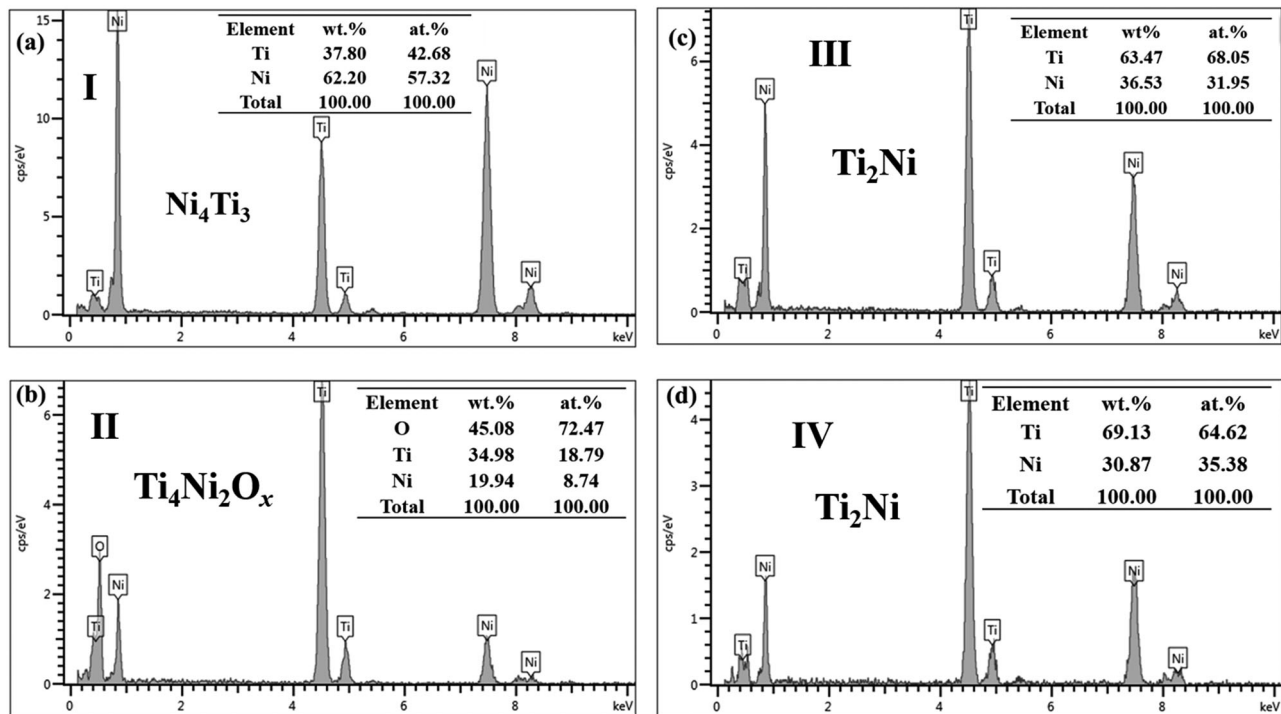
Figure 7. TEM-EDS results of (a) lath clusters in region I and different nanoprecipitates in (b) region II, (c) region III, and (d) region IV in the function domain of the modified NiTi in Figure 6.

Further, high-resolution TEM and its inverse fast Fourier transform (IFFT) image revealed that 1–3 nm Ni_4Ti_3 clusters were distributed homogeneously in the interior of B2 grains (Figure 6d), and there was a distinct lattice distortion at the Ni_4Ti_3/B2 interface. Meanwhile, TEM-EDS confirmed that the composition of these lath clusters in Figure 7a was consistent with Ni_4Ti_3 phase. Besides, it should be noted that there existed another kind of nanoprecipitate in the HAZ (region II in Figure 6a), and corresponding EDS results proved that it is $Ti_4Ni_2O_x$ phase (Figure 7b).

In the TZ and CGZ, TEM-EDS results in Figure 7c and d found that there was no obvious oxygen in these nanoprecipitates (regions III and IV in Figure 6c and e), and the compositions of these nanoprecipitates were closed to Ti_2Ni phase. Thus, in this work, these nanoprecipitates in the TZ and CGZ were considered to be Ti_2Ni. Similar Ti_2Ni nanoprecipitates also had been observed and confirmed by TEM-EDS compositional analysis in prior work by (Franco et al. 2017). Figure 6c shows that Ti_2Ni nanoprecipitates (8–18 nm) formed in B2 grain interior (arrows in Figure 6b). These Ti_2Ni nanoprecipitates were smaller than those in the as-atomised NiTi, indicating that the addition of Ni nanoparticles could inhibit the growth of the Ti_2Ni phase. The corresponding SAED patterns were indexed to the B2 matrix and cubic Ti_2Ni along $[1\bar{1}0]_{B2}$ (Figure 6e). In the CGZ, Ti_2Ni nanoprecipitates 30–45 nm in diameter

were distributed along the B2 grain boundaries (Figure 6c and f).

It is known that the types of precipitates in NiTi SMAs can significantly affect the corresponding interface type. In this study, the interface between the Ni_4Ti_3 lath clusters and B2 matrix in the HAZ was coherent, and the interface between the Ti_2Ni nanoprecipitates and B2 matrix in the TZ was semi-coherent, as confirmed by (Tomozawa, Kim, and Miyazaki 2009). Owing to the larger quantity of defects in the grain boundaries in the CGZ, it can be deduced that the mismatch of the corresponding interface between the Ti_2Ni nanoprecipitates and B2 matrix was greater than that in the TZ. Reasonably, different interfaces would lead to different interaction mechanisms between precipitates and dislocations formed during mechanical loading, thereby resulting in different mechanical responses. Importantly, it should be noted that the HAZ and the TZ and CGZ in the modified NiTi were unique locations for the precipitation of Ni_4Ti_3 lath clusters and Ti_2Ni nanoprecipitates, respectively. The related mechanisms will be discussed in Section 4.1.

3.3. Mechanical responses of AMed NiTi SMAs

Figure 8 shows the cyclic thermomechanical stress–strain curves and variations in the recovery and residual strains with number of cycles for the as-atomised and
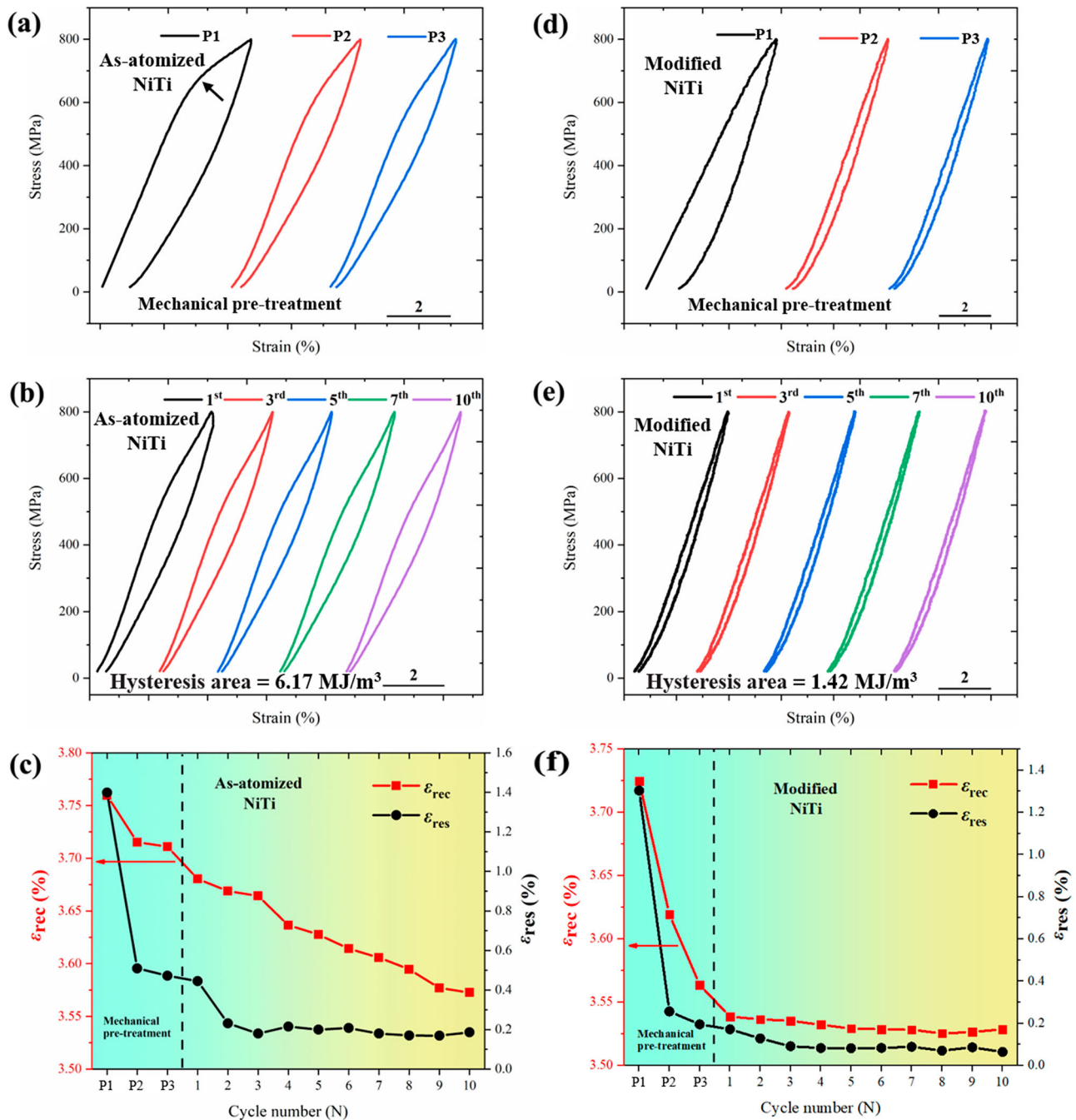
Figure 8. Cyclic thermomechanical properties. (a, b, d, e) Cyclic thermomechanical stress–strain curves and (c, f) variation in the recovery strain (ε_{rec}) and residual strain (ε_{res}) with number of cycles for the ⌀3 × 6 mm cylindrical specimens of the as-atomised (a–c) and modified (d–f) NiTi at A_f + 10°C and 800 MPa.

modified NiTi at A_f + 10°C. To eliminate the effect of unavoidable micropores formed during AM and consequently attain better reversibility of the thermomechanical responses during loading and unloading, three mechanical pre-treatments were conducted for the two NiTi (P1–P3 in Figure 8a and d) (Hou et al. 2019). Specifically, P1, P2 and P3 was the first, second and third pre-treatment, respectively. After the mechanical pre-treatments, the average hysteresis areas

during cyclic thermomechanical tests were 6.17 and 1.42 MJ/m³ for the as-atomised and modified NiTi (Figure 8b and e), respectively. Although both samples had been pre-treated, it should be noted that the recovery strain (ε_{rec}) of as-atomised NiTi decreased obviously (Figure 8c), and the ε_{rec} of modified NiTi stabilised at ~3.54%. Besides, the residual strain (ε_{res}) of as-atomised and modified NiTi at every cycle after the pre-treatment were about 0.2% and 0.1%, respectively.
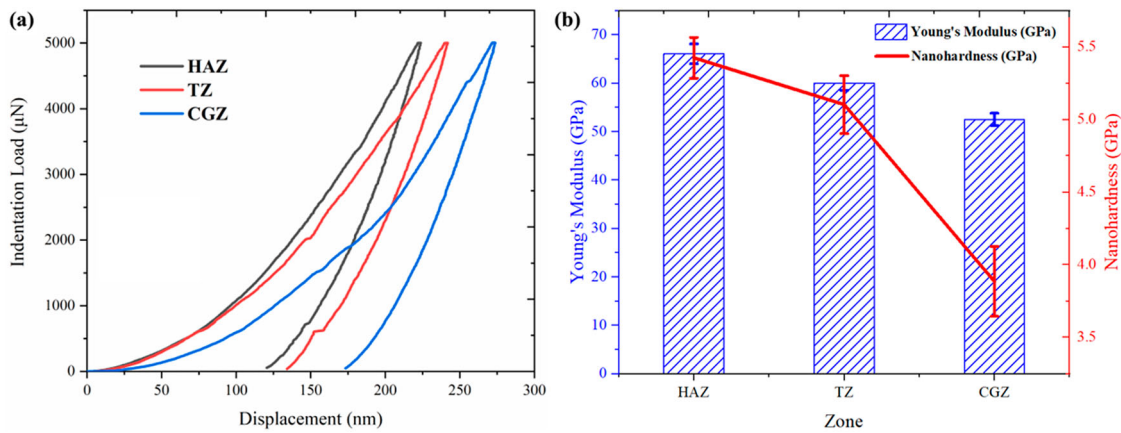
Figure 9. (a) Displacement–load curves and (b) Young's modulus and nanohardness from nanoindentation analysis of the three characteristic zones in the function domain of the modified NiTi.

Figure 9 shows the displacement–load curves, Young's moduli, and nanohardness values of the three characteristic zones in the function domain of the modified NiTi. The three zones exhibited graded mechanical properties. Specifically, the Young's modulus and nanohardness decreased gradually from the HAZ (66.1 and 5.4 GPa, respectively) to the TZ (60.0 and 5.1 GPa, respectively) and the CGZ (52.5 and 3.9 GPa, respectively), as shown in Figure 9b. The gradient in the Young's modulus is attributed to the different Ni_4Ti_3 and Ti_2Ni precipitates in the different zones. The Ni_4Ti_3 precipitates in the HAZ had a higher Young's modulus (108 GPa [Wagner and Windl 2009]) than that of the Ti_2Ni precipitates in the TZ and CGZ (44.4 GPa [Toprek, Belosevic-Cavor, and Koteski 2015]). Furthermore, the gradient in the nanohardness is attributed to precipitation hardening due to a gradient in the particle size of the Ni_4Ti_3 and Ti_2Ni precipitates (Figure 6) (1–3 nm Ni_4Ti_3 clusters in the grain interior of B2 austenite in the HAZ, 8–18 nm Ti_2Ni precipitates in the grain interior of B2 austenite in the TZ, and 30–45 nm Ti_2Ni precipitates along the grain boundaries of B2 austenite in the CGZ).

4. Discussion

4.1. Formation mechanism of Ni_4Ti_3 and Ti_2Ni precipitates at different locations in the function domain

Figure 10a shows simulated 3D temperature fields for the laser track at 10.5 ms during AM. These simulation results were based on the conservation laws of fluid dynamics and discretized in a regular 3D spatial array in Cartesian coordinates; the complicated physical processes (such as melting, phase change, and melt pool flow) during AM were numerically solved using computational fluid dynamics, as stated by (Yan et al. 2017). The simulated depths and widths of the melt pools were 95 and 130 μm, respectively. These values agree well with the corresponding values obtained from the optical contours from side views of the melt pools in the modified NiTi (85 and 135 μm, respectively; Figure 10b inset), which validates the simulation results.

Figure 10b shows a longitudinal sectional view of heat transfer and fluid flow in the melt pool at 11.3 ms during the AM process; here, fluid flow is represented by black arrows. Near the melt-pool surface, the metal melt was pulled from the centre to the rear of the melt pool owing to temperature-dependent surface tension (Cho et al. 2009). The centre was heated to a temperature higher than that at the rear. As a result, the surface tension was lower at the centre than that at the rear, which drove the metal melt flow backward near the surface. Furthermore, a sufficiently strong backward flow can result in an anticlockwise pattern, in which the metal melt returns from the rear to the centre inside the melt pool. The backward flow near the melt-pool surface resulted in a surface profile that was depressed underneath the laser beam and raised toward the rear of the melt pool. This mounded shape led to the formation of spatter powder on the surfaces of the AMed bulk alloys (Figure 2a and b). The approximate locations of the three characteristic zones in the function domain are shown in Figure 10c. The melt-pool boundary is marked by dotted isotherm lines at 1583 K, which is the liquidus temperature of the NiTi SMAs (Table 1).

Figure 10d shows the temperature–time plots at different positions at a depth of 45 μm inside the function domain. The temperature fluctuations were extremely large at these positions, which correspond to the thermal history at different positions inside the function domain (Figure 10c), specifically in the HAZ, TZ, and CGZ.
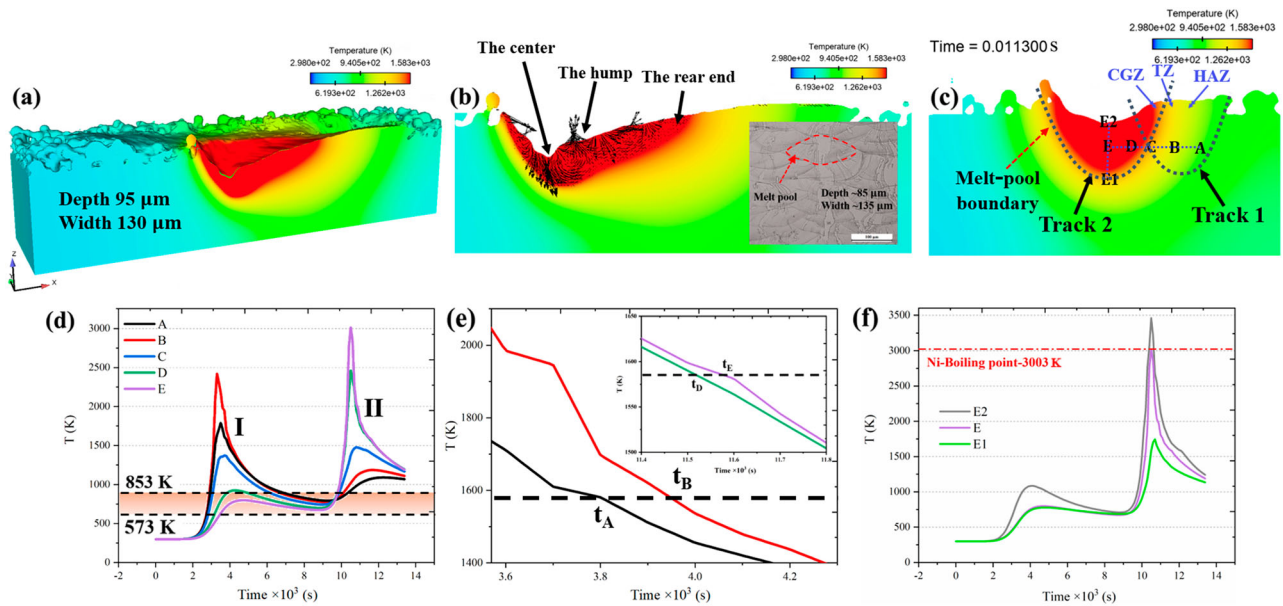
Figure 10. (a) Simulated 3D temperature fields for the laser track at 10.5 ms during AM. (b) Longitudinal sectional view of heat transfer and fluid flow in the melt pool at 11.3 ms and optical contours from the side view of melt pools in the modified NiTi. (c) Temperature fields for the second laser track and cross-sectional view of two adjacent laser tracks. Note that a function domain containing the HAZ, TZ, and CGZ is constructed between two adjacent melt pools. (d) Temperature–time plots at different positions at a depth of 45 μm inside the function domain: positions A and B are inside the HAZ, position C is inside the CGZ, and positions D and E are inside the melt pool. The spacing between two adjacent positions is ~20 μm. (e) Solidification temperature–time plots at different positions inside the function domain ($t_A < t_B$ and $t_D < t_E$). (f) Temperature–time plots at different depths in the centre of the second melt pool (E1: 80 μm, E: 45 μm, and E2: 5 μm).

Figure 10e shows the solidification temperature–time plots at various positions inside the function domain. Based on the different solidification time intervals, it was found that the melt pool solidified from the boundary and moved toward the centre, that is, from positions A to B and D to E. The maximum solidification rate was observed at the melt-pool boundaries along with a high nucleation rate, which resulted in the formation of ultrafine cellular grains (Figures 3f and 4c). Figure 10f shows the temperature–time plots at various locations at different depths. The temperature at position E2, corresponding to the surface of the melt pool, exceeded the boiling point of Ni (3003 K). This caused Ni depletion during the AM process, which is consistent with the EDS results in Figure 2 and the differences in the chemical composition of the initial NiTi SMA powder and AMed bulk alloys, as found by (Sam et al. 2018).

Theoretically, the formation of Ni_4Ti_3 and Ti_2Ni precipitates in different characteristic zones in the modified NiTi can be explained based on the thermal history of two adjacent laser tracks. (Kim and Miyazaki 2005) found that a suitable heat-treatment temperature range (573–873 K) and holding time are key factors dictating the nucleation and growth of Ni_4Ti_3 precipitates. Specifically, in $Ni_{50.9}Ti_{49.1}$ SMAs, Ni_4Ti_3 precipitates cannot form at a low aging temperature (373 K), even

after an extended holding time of 10,800 ks; however, they begin to form when the aging temperature exceeds 473 K and the holding time is 360 ks, and they require an even shorter holding time of 1.2 ks at 573 K. Furthermore, (Khalil-Allafi, Dlouhy, and Eggeler 2002) also reported that at higher aging temperatures (673 → 773 → 823 K) and longer aging times (3.6 → 36 ks), large Ni_4Ti_3 precipitates can form in $Ni_{50.7}Ti_{49.3}$ SMAs. Figure 11 shows diagrams of the orderly construction the function domain in the modified NiTi during AM. Figure 11b shows the distribution of the function domain along the side surface. Since the internal of the melt pools would undergo the similar thermal histories at different depths of adjacent two melt pools. It is reasonable that similar orderly microstructure would be obtained along the side surface at two adjacent melt pools. Based on the Ni–Ti binary phase diagram, Ni atoms have a greater degree of supersaturation in NiTi than that of Ti atoms at a given temperature (>680°C) (Otsuka and Ren 2005). For a single laser track in the AM process, only Ti_2Ni precipitates or Ti-rich concentrations formed owing to the high solidification rate, no thermal history, and greater supersaturation of Ni atoms in NiTi (Figure 11a). The interaction between two adjacent laser tracks or melt pools resulted in the formation of a HAZ and TZ in previous melt pools and

the associated CGZ in subsequent melt pools (Figure 11b). This gave rise to the formation of the three characteristic zones (HAZ, TZ, and CGZ) and the formation of orderly constructed function domains. The width of the function domain in this study was 90–110 μm, which was consistent between the simulated and experimental results. As shown in Figure 10c, the previously deposited laser track underwent a thermal cycle due to the subsequent laser track. This resulted in the formation of the HAZ, which experienced a specific thermal history from 573 to 873 K (Figure 10d). This made it possible to ensure an exact temperature range suitable for the nucleation of Ni_4Ti_3. It should be noted that the duration corresponding to the temperature window (573–873 K) was only several milliseconds (Figure 10d). Because this short duration was insufficient to promote the growth of Ni_4Ti_3, only extremely fine Ni_4Ti_3 lath clusters (1–3 nm) formed in the HAZ (Figure 6a).

For the Ti_2Ni precipitates, the formation mechanism is associated with the solidification rate and solid solubility of Ti atoms in B2 austenite. Generally, a higher solidification rate promotes the formation of Ti_2Ni in NiTi SMAs, as researched by (Nagarajan and Chattopadhyay 1994), while a high cooling rate results in the formation of a supersaturated solid solution. This means that supersaturated Ti atoms were concentrated in local areas and more likely to precipitate, thereby acting as nucleation sites to form the Ti_2Ni phase (Figure 11a). Comparing

the CGZ and TZ in the function domain (Figure 10c), the edge of the melt pool had a shorter melt duration and faster solidification time, which promoted nucleation of grains and the formation of ultrafine cellular grains. It should be noted that the CGZ was located precisely in the overlapping region between two adjacent laser tracks. This indicates that the CGZ underwent two melting cycles during the AM process. The Ti_2Ni or concentrated Ti atoms formed during the initial melting acted as nucleation sites, resulting in Ti_2Ni nanoprecipitates distributed along the grain boundaries of the CGZ (Figure 6), similar to those in AMed $Ni_{49.6}Ti_{50.4}$ (Lu et al. 2019) and $Ni_{51.3}Ti_{48.7}$ (Zhou et al. 2019). Furthermore, the Ti_2Ni or concentrated Ti atoms formed during the initial melting in the TZ underwent a thermal cycle due to the subsequent laser track (Track 2 in Figures 10c and 11b). Because the TZ was next to the CGZ, it underwent a higher temperature thermal cycle relative to that of the HAZ. The faster diffusion of Ti atoms in the supersaturated B2 solid solution and higher temperature thermal cycle led to the formation of more Ti_2Ni nanoprecipitates in the grain interior of the TZ (Figure 6). These explanations are supported by the larger Ti_2Ni precipitates in the TZ relative to those in the HAZ in the as-atomised NiTi (Figure 3g–i). Besides, based on Figures 6 and 7, it can be found that some $Ti_4Ni_2O_x$ nanoprecipitates formed in the HAZ, similar to that in AMed $Ni_{50.6}Ti_{49.4}$ SMAs (Gu et al. 2021). It can be inferred that the relatively more $Ti_4Ni_2O_x$ nanoprecipitates in the

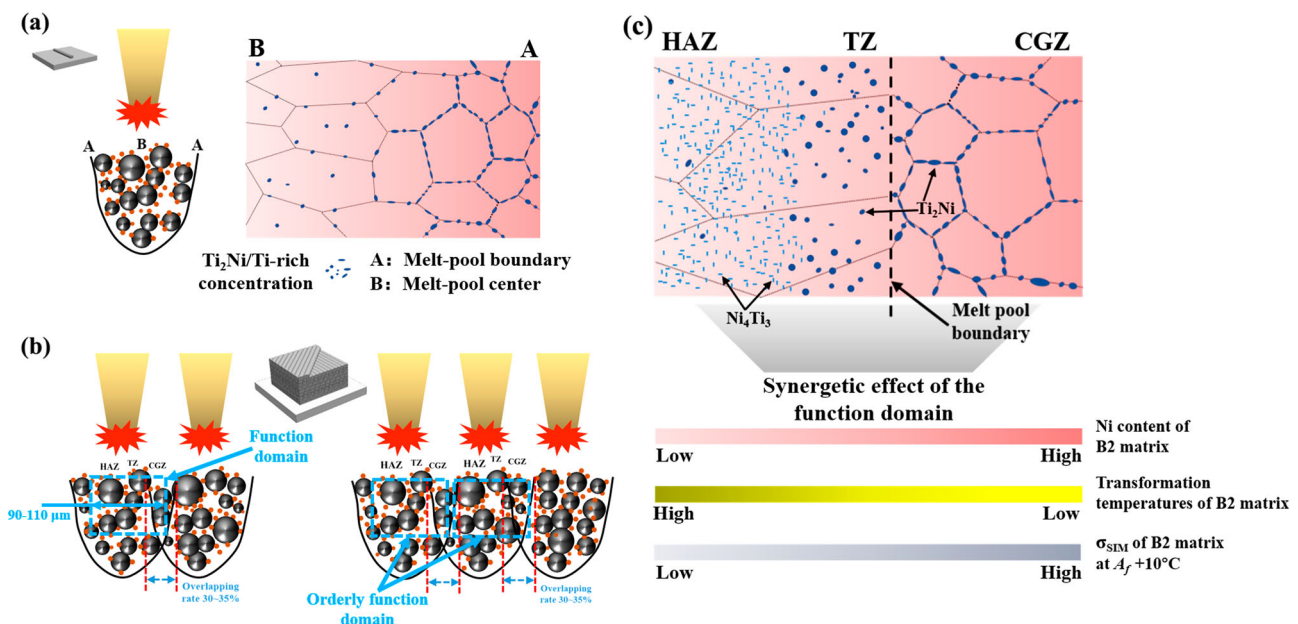**Figure 11.** Orderly construction of the function domain and its synergetic effect on the thermomechanical responses of the modified NiTi. (a) Microstructural evolution inside a single laser track, (b) orderly construction of the function domain with the three characteristic zones by multiple laser tracks, and (c) synergetic effect of the orderly constructed function domain on thermomechanical responses of the modified NiTi.

HAZ was ascribed to the longer solidification time and higher temperature in the HAZ (the centre of melt pool, Figure 10f) during AM relative to other two zones (TZ and CGZ), which induced more oxygen atoms in the modified NiTi and thus the formation of $Ti_4Ni_2O_x$ in the HAZ (Figure 6a).

4.2. Synergetic effect of the three characteristic zones in the function domain

Based on the TEM images and EDS results of the as-atomised NiTi (Figures 3 and 5), the same nanoprecipitates (Ti_2Ni) formed in the three characteristic zones. Therefore, the Ni content of the B2 matrix in the as-atomised NiTi was relatively homogeneous. Thus, the stress-induced B2 → B19′ transformation occurred simultaneously in the three zones of the as-atomised NiTi, resulting in an evident transformation demarcation point (black arrow in Figure 8a) and a larger recovery strain than that of the modified NiTi (Figure 8c and f). In addition, the stable residual strain of the as-atomised NiTi, ∼0.2% (Figure 8c), was almost twice than that of the modified NiTi (∼0.1%, Figure 8f). This is attributed to the stronger destructive effect of the grain-boundary Ti_2Ni nanoprecipitates in the CGZ (Figure 3i), which constituted a larger proportion of the function domain in as-atomised NiTi (30%) than that in the modified NiTi (18%). During the loading process, an increasing number of dislocations formed in the matrix and subsequently piled up at the grain boundaries of CGZ, generating a large internal stress to resist external stress (Kang et al. 2021). Furthermore, stress concentrations occurred easily at grain boundaries with Ti_2Ni nanoprecipitates (Johnson et al. 2019). Once the internal stress and stress concentration exceeded the strength of the grain boundaries, they were destroyed, thereby resulting in a rapid increase in residual strain (Luo et al. 2021). In addition, previous studies by (Ishida et al. 1995; Tomozawa, Kim, and Miyazaki 2009) found that the recovery strain of a $Ni_{48.2}Ti_{51.8}$ film decreased with the increasing size of Ti_2Ni nanoprecipitates. Thus, the higher proportion of the CGZ and the larger Ti_2Ni nanoprecipitates in the as-atomised NiTi relative to the modified NiTi resulted in a more obvious decrease in the recovery strain (Figure 8c). Besides, in the HAZ of the modified NiTi, a large number of Ni_4Ti_3 nanoclusters (1–3 nm) were homogeneously distributed in the B2 grain interior (Figure 6a and d), and had coherent interface with B2 matrix. During cyclic thermomechanical loading, although high-density dislocations would be formed in the matrix of NiTi, these Ni_4Ti_3 clusters and Ti_2Ni nanoprecipitates would impede the movement of the formed

dislocations effectively, and consequently enhance the strength of the matrix.

On the one hand, compared with the as-atomised NiTi, the modified NiTi exhibited a more stable recovery strain of ∼3.54% (Figure 8f) and a smaller hysteresis area of 1.42 MJ/m^3 (Figure 8e) during 10 compression cycles. Three effective methods for obtaining a stable recovery strain in NiTi SMAs have been documented: saturating dislocations formed in the B2 matrix, forming Ni_4Ti_3 nanoprecipitates, and refining B2 grains to suppress the generation of dislocations, as confirmed by (Ahadi and Sun 2015; Wang et al. 2015). In this study, the orderly melt-pool construction during AM (Figures 2 and 11b) resulted in the formation of an ordered function domain containing the HAZ, TZ, and CGZ. Figure 11c shows the variation in the physical properties of the orderly constructed function domain and its synergetic effect on the thermomechanical responses of the modified NiTi. Based on the EDS results in Figure 5, Ni and Ti were distributed homogeneously in the function domain in the modified NiTi at the micrometer scale for all the characteristic zones. Nevertheless, owing to the different precipitates in the three zones (Figure 6a–c) (1–3 nm Ni_4Ti_3 clusters in the B2 grain interior in the HAZ, 8–18 nm Ti_2Ni precipitates in the B2 grain interior in the TZ, and 30–45 nm Ti_2Ni precipitates along the B2 grain boundaries in the CGZ), the Ni content of the B2 matrix increased gradually from the HAZ to the TZ and CGZ. Because the B2 → B19′ transformation temperature in NiTi SMAs decreases with increasing Ni content (Frenzel et al. 2010), a sequential phase transformation occurred in the function domain during the cooling and heating processes. As a result, the modified NiTi had a wider A_f–A_s range (Figure 2d). According to the Clausius–Clapeyron relation, the critical stress for B2 → B19′ is strongly dependent on the test temperature with a positive slope. Note that the B2 → B19′ transformation temperature decreased from the HAZ to the TZ and CGZ. Therefore, at the test temperature (A_f + 10℃), the σ_{SIM} of the B2 matrix increased gradually from the HAZ to the TZ and CGZ (Figure 11c). Also, this point also had been supported by the gradually decreased grain size from the HAZ to the TZ and CGZ (Figure 6a–c) (Ahadi and Sun 2014). During the cyclic compression of the modified NiTi, the highest σ_{SIM} of the CGZ inhibited the formation of new dislocations during the B2 → B19′ transformation, while the relatively low σ_{SIM} of the TZ and HAZ accommodated the formation of more dislocations during the loading process. The movement of these formed dislocations was impeded by the homogeneously distributed Ti_2Ni nanoprecipitates and Ni_4Ti_3 clusters in the B2 grain interior of the TZ and HAZ (Figure 6a and b). In

addition, the propagation of preferential destruction in the CGZ due to its grain-boundary Ti_2Ni nanoprecipitates was restrained by the TZ and HAZ. In summary, the formation of Ni_4Ti_3 clusters, small Ti_2Ni nanoprecipitates and inhibition of dislocation generation in the three zones in the orderly constructed function domain stabilised the recovery stain during cyclic compression of the modified NiTi (Figures 8d and 11c).

On the other hand, the smaller hysteresis area of the modified NiTi (Figure 8b and e) is ascribed to the sequential occurrence of the stress-induced B2 → B19′ transformation in the function domain. In general, the introduction of dislocations and residual nanoscale martensite and the formation of a non-transformable phase reduce the hysteresis area. As depicted in Figure 11c, the σ_{SIM} of the B2 matrix at $A_f + 10°C$ increased from the HAZ to the TZ and CGZ. The B2 matrix in the TZ and CGZ had a higher σ_{SIM} relative to that of the HAZ, and thus the HAZ, TZ and CGZ underwent the stress-induced martensite transformation orderly during loading. Therefore, the TZ and CGZ could act as non-transformable zones during the occurrence of stress-induced martensite transformation in the HAZ, which effectively contributed to the decrease in the hysteresis area of the modified NiTi. In addition, the high-density coherent Ni_4Ti_3 clusters and relatively small Ti_2Ni nanoprecipitates in the modified NiTi strongly hindered the interface movement of the formed martensite. This indicates that continuous loading stress was required to induce the stress-induced martensite transformation, which is supported by the absence of an evident transformation point (Figure 8d). In contrast, the as-atomised NiTi had the same Ti_2Ni nanoprecipitates (Figure 3g–i) and a homogeneous Ni distribution in the B2 matrix in the three zones (Figure 5). This induced a simultaneous B2 → B19′ transformation in the three zones of the as-atomised NiTi during loading, which is supported by the evident transformation point (black arrow in Figure 8a). Therefore, the high-density Ni_4Ti_3 clusters and Ti_2Ni nanoprecipitates in the HAZ and TZ (Figure 6a and b) and orderly occurrence of stress-induced martensite transformation in the HAZ, TZ and CGZ during loading resulted in a smaller hysteresis area for the modified NiTi than that of the as-atomised NiTi.

5. Conclusions

In this study, a modified $Ni_{50.6}Ti_{49.4}$ powder was obtained by adding uniform Ni nanoparticles to as-atomised $Ni_{49.6}Ti_{50.4}$ powder, and a novel ordered function domain was found in AMed $Ni_{50.6}Ti_{49.4}$ SMAs. The main conclusions of this investigation are as follows:

(1) The modified $Ni_{50.6}Ti_{49.4}$ powder, which was produced by low-energy ball milling of as-atomised $Ni_{49.4}Ti_{50.6}$ powder and Ni nanoparticles, had a particle-size distribution identical to that of the as-atomised powder, while its laser reflectivity was 7.8% lower than that of the as-atomised powder. The uniform distribution of Ni nanoparticles on the surfaces of the modified powder particles was due to their opposite zeta potentials.

(2) The orderly constructed function domain in the AMed $Ni_{50.6}Ti_{49.4}$ contained three characteristic zones: the HAZ, TZ, and CGZ. Although the matrix in all these zones was B2 austenite, they exhibited inhomogeneous precipitation behaviour, with 1–3 nm Ni_4Ti_3 precipitates in the grain interior of the HAZ, 8–18 nm Ti_2Ni precipitates in the grain interior of the TZ, and 30–45 nm Ti_2Ni precipitates along the grain boundaries in the CGZ, which can be explained by the specific thermal histories of the three zones.

(3) Cyclic compression at $A_f + 10°C$ demonstrated that the AMed $Ni_{50.6}Ti_{49.4}$ exhibited a more stable recovery strain and smaller hysteresis area than those of the AMed $Ni_{49.6}Ti_{50.4}$. The more stable recovery strain is attributed to the formation of Ni_4Ti_3 clusters, small Ti_2Ni nanoprecipitates and inhibition of dislocation generation in the three zones. Furthermore, the smaller hysteresis area originated from the high-density clusters and nanoprecipitates in the HAZ and TZ and the orderly occurrence of stress-induced martensite transformation in the HAZ, TZ and CGZ during loading.

Disclosure statement

Funding

Notes on contributors

H. Z. Lu received his bachelor degree from Wuhan University of Science and Technology at 2016. He is currently working toward his Ph.D. thesis on functional properties of NiTi shape memory alloys fabricated by laser powder bed fusion process at South China University of Technology. His research includes NiTi shape memory alloys, titanium alloys, and Ti-based shape memory alloys.

T. Chen received his bachelor degree in school of mechanical & automotive engineering in 2017 from South China University of

Technology. He is currently working toward his Ph.D. thesis on fabricating of titanium composites with high mechanical performance, at National Engineering Research Center of Near-net-shape Forming for Metallic Materials, South China University of Technology. his research includes additive manufacturing and powder sintering of Ti alloys and composites.

L. H. Liu received PhD degree in mechanical engineering from Tsinghua University at 2019. Currently, he is a postdoctoral researcher at National Engineering Research Center of Near-Net-Shape Forming for Metallic Materials in South China University of Technology. His research interests mainly include bulk metallic glasses, titanium alloys and high-entropy alloys.

H. Wang received his Ph.D. degree from Georgia Institute of Technology in 2010. He is currently an associate professor in Shenzhen University. His research interests focus on laser and additive manufacturing, amorphous alloys and high entropy alloys, two-dimensional nanomaterials and micro-nano devices.

X. Luo received his bachelor degree in school of mechatronics engineering in 2016 from Nanchang University. He is currently working toward his Ph.D. thesis on microstructure, mechanical properties, corrosion resistance, and biocompatibility of Si alloying biomedical β-type titanium alloy produced by additive manufacturing, at National Engineering Research Center of Near-net-shape Forming for Metallic Materials, South China University of Technology.

C. H. Song is currently an associate professor and deputy director at the School of Mechanical and Automotive Engineering, South China University of Technology. He has been engaged in LPBF research since 2009 and received his PhD at 2014. He completed the development of the fourth generation LPBF metal 3D printing equipment. At present, his research focuses on multi-field assisted LPBF additive manufacturing and structural performance regulation of metal materials in medical and nuclear power fields.

Z. Wang is a full professor in the School of Mechanical and Automotive Engineering, South China University of Technology, China. After receiving his Ph.D. at Dresden University of Technology, Germany, in 2014, Dr. Wang had worked in AIMR at Tohoku University, Japan, from 2014 to 2016. His current research interest is focused on aluminum alloys, titanium alloys, and their composites with relatively low density and high mechanical performance produced by powder metallurgy, casting and additive manufacturing techniques.

C. Yang is a professor and director of Metallic Materials Institute of Forming Technology and Equipments (National Engineering Research Center of Near-net-shape Forming for Metallic Materials) at South China University of Technology, China. His research team specializes in metal metallurgical processing, including microstructure-properties interrelation, forming technology (additive manufacturing, powder sintering, and pressure casting, etc.) and engineering applications of various metallic alloys and their components (shape memory alloy, advanced titanium alloy, and lead-free brass alloy, etc.).

References

Ahadi, A., and Q. Sun. 2014. "Effects of Grain Size on the Rate-Dependent Thermomechanical Responses of Nanostructured Superelastic NiTi." *Acta Materialia* 76: 186–197. https://doi.org/10.1016/j.actamat.2014.05.007.

Ahadi, A., and Q. Sun. 2015. "Stress-induced Nanoscale Phase Transition in Superelastic NiTi by in Situ X-ray Diffraction." *Acta Materialia* 90: 272–281. https://doi.org/10.1016/j.actamat.2015.02.024.

Alagha, A. N., S. Hussain, and W. Zaki. 2021. "Additive Manufacturing of Shape Memory Alloys: A Review with Emphasis on Powder Bed Systems." *Materials & Design* 204: 109654. https://doi.org/10.1016/j.matdes.2021.109654.

Brandes, E. A., and G. B. Brook. 1983. "Smithells Metals Reference Book, Sixth Edition".

Cao, Y., X. Zhou, D. Cong, H. Zheng, Y. Cao, Z. Nie, Z. Chen, et al. 2020. "Large Tunable Elastocaloric Effect in Additively Manufactured Ni–Ti Shape Memory Alloys." *Acta Materialia* 194: 178–189. https://doi.org/10.1016/j.actamat.2020.04.007.

Chen, H., F. Xiao, X. Liang, Z. Li, Zhu Li, X. Jin, N. Min, and T. Fukuda. 2019. "Improvement of the Stability of Superelasticity and Elastocaloric Effect of a Ni-Rich Ti-Ni Alloy by Precipitation and Grain Refinement." *Scripta Materialia* 162: 230–234. https://doi.org/10.1016/j.scriptamat.2018.11.024.

Cho, J. H., D. F. Farson, J. O. Milewski, and K. J. Hollis. 2009. "Weld Pool Flows During Initial Stages of Keyhole Formation in Laser Welding." *Journal of Physics D: Applied Physics* 42 (17): 175502. https://doi.org/10.1088/0022-3727/42/17/175502.

Chu, K., and Q. Sun. 2021. "Reducing Functional Fatigue, Transition Stress and Hysteresis of NiTi Micropillars by one-Step Overstressed Plastic Deformation." *Scripta Materialia* 201: 113958. https://doi.org/10.1016/j.scriptamat.2021.113958.

Committe, A. 1990. *ASM Handbook, Properties and Selection: Nonferrous Alloys and Special-Purpose Materials. vol. 2.* ASM International.

Elahinia, Mohammad H., Mahdi Hashemi, Majid Tabesh, and Sarit B. Bhaduri. 2012. "Manufacturing and Processing of NiTi Implants: A Review." *Progress in Materials Science* 57 (5): 911–946. https://doi.org/10.1016/j.pmatsci.2011.11.001.

Elahinia, M., N. S. Moghaddam, M. T. Andani, A. Amerinatanzi, B. A. Bimber, and R. F. Hamilton. 2016. "Fabrication of NiTi Through Additive Manufacturing: A Review." *Progress in Materials Science* 83: 630–663. https://doi.org/10.1016/j.pmatsci.2016.08.001.

Fereiduni, E., A. Ghasemi, and M. Elbestawi. 2019. "Selective Laser Melting of Hybrid ex-Situ/in-Situ Reinforced Titanium Matrix Composites: Laser/Powder Interaction, Reinforcement Formation Mechanism, and non-Equilibrium Microstructural Evolutions." *Materials & Design* 108185. https://doi.org/10.1016/j.matdes.2019.108185.

Franco, B. E., J. Ma, B. Loveall, G. A. Tapia, K. Karayagiz, J. Liu, A. Elwany, R. Arroyave, and I. Karaman. 2017. "A Sensory Material Approach for Reducing Variability in Additively Manufactured Metal Parts." *Scientific Reports* 7 (1): 3604. https://doi.org/10.1038/s41598-017-03499-x.

Frenzel, J., E. P. George, A. Dlouhy, Ch Somsen, M. F. X. Wagner, and G. Eggeler. 2010. "Influence of Ni on Martensitic Phase Transformations in NiTi Shape Memory Alloys." *Acta Materialia* 58 (9): 3444–3458. https://doi.org/10.1016/j.actamat.2010.02.019.

Gu, D., C. Ma, D. Dai, J. Yang, K. Lin, H. Zhang, and H. Zhang. 2021a. "Additively Manufacturing-Enabled Hierarchical NiTi-Based Shape Memory Alloys with High Strength and Toughness." *Virtual and Physical Prototyping*, 1–20. https://doi.org/10.1080/17452759.2021.1892389.

Gu, D., X. Shi, R. Poprawe, D. L. Bourell, R. Setchi, and J. Zhu. 2021b. "Material-Structure-Performance Integrated Laser-Metal Additive Manufacturing." *Science* 372 (6545). https://doi.org/10.1126/science.abg1487.

Guo, Y., Y. Zhao, S. Wang, C. Jiang, and J. Zhang. 2018. "Relationship Between the Zeta Potential and the Chemical Agglomeration Efficiency of Fine Particles in Flue gas During Coal Combustion." *Fuel* 215: 756–765. https://doi.org/10.1016/j.fuel.2017.11.005.

Herzog, D., V. Seyda, E. Wycisk, and C. Emmelmann. 2016. "Additive Manufacturing of Metals." *Acta Materialia* 117: 371–392. https://doi.org/10.1016/j.actamat.2016.07.019.

Hossain, A. A., M. Yang, A. Checco, G. Doerk, and C. E. Colosqui. 2020. "Large-area Nanostructured Surfaces with Tunable Zeta Potentials." *Applied Materials Today* 19: 100553. https://doi.org/10.1016/j.apmt.2019.100553.

Hou, H., E. Simsek, T. Ma, N. S. Johnson, S. Qian, C. Cissé, D. Stasak, et al. 2019. "Fatigue-resistant High-Performance Elastocaloric Materials Made by Additive Manufacturing." *Science* 366 (6469): 1116–1121. https://doi.org/10.1126/science.aax7616.

Ishida, A., M. Sato, A. Takei, and Miyazaki, S. 1995. "Effect of Heat Treatment on Shape Memory Behavior of Ti-Rich Ti–Ni Thin Films." *Materials Transactions, JIM* 36 (11): 1349–1355.

Jani, J. M., M. Leary, A. Subic, and M. A. Gibson. 2014. "A Review of Shape Memory Alloy Research, Applications and Opportunities." *Materials & Design (1980-2015)* 56: 1078–1113. https://doi.org/10.1016/j.matdes.2013.11.084.

Johnson, D. C., B. Kuhr, D. Farkas, and G. S. Was. 2019. "Quantitative Linkage Between the Stress at Dislocation Channel – Grain Boundary Interaction Sites and Irradiation Assisted Stress Corrosion Crack Initiation." *Acta Materialia* 170: 166–175. https://doi.org/10.1016/j.actamat.2019.02.032.

Kang, L. M., Y. J. Cai, X. C. Luo, Z. J. Li, X. B. Liu, Z. Wang, Y. Y. Li, and C. Yang. 2021. "Bimorphic Microstructure in Ti-6Al-4V Alloy Manipulated by Spark Plasma Sintering and in-Situ Press Forging." *Scripta Materialia* 193: 43–48. https://doi.org/10.1016/j.scriptamat.2020.10.035.

Khalil-Allafi, J., A. Dlouhy, and G. Eggeler. 2002. "Ni$_4$Ti$_3$-precipitation During Aging of NiTi Shape Memory Alloys and its Influence on Martensitic Phase Transformations." *Acta Materialia* 50 (17): 4255–4274.

Kim, J., and S. Miyazaki. 2005. "Effect of Nano-Scaled Precipitates on Shape Memory Behavior of Ti-50.9at.%Ni Alloy." *Acta Materialia* 53 (17): 4545–4554. https://doi.org/10.1016/j.actamat.2005.06.009.

Kou, S. 2002. "Welding Metallurgy, Second Edition".

Lee, Y. S., and W. Zhang. 2016. "Modeling of Heat Transfer, Fluid Flow and Solidification Microstructure of Nickel-Base Superalloy Fabricated by Laser Powder Bed Fusion." *Additive Manufacturing* 12: 178–188. https://doi.org/10.1016/j.addma.2016.05.003.

Li, X. P., G. Ji, Z. Chen, A. Addad, Y. Wu, H. W. Wang, J. Vleugels, J. Van Humbeeck, and J. P. Kruth. 2017. "Selective Laser Melting of Nano-TiB$_2$ Decorated AlSi10Mg Alloy with High Fracture Strength and Ductility." *Acta Materialia* 129: 183–193. https://doi.org/10.1016/j.actamat.2017.02.062.

Li, B., B. Qian, Y. Xu, Z. Liu, J. Zhang, and F. Xuan. 2019. "Additive Manufacturing of Ultrafine-Grained Austenitic Stainless Steel Matrix Composite via Vanadium Carbide Reinforcement Addition and Selective Laser Melting: Formation Mechanism and Strengthening Effect." *Materials Science and Engineering: A* 745: 495–508. https://doi.org/10.1016/j.msea.2019.01.008.

Lu, B., X. Cui, W. Ma, M. Dong, Y. Fang, X. Wen, G. Jin, and D. Zeng. 2020. "Promoting the Heterogeneous Nucleation and the Functional Properties of Directed Energy Deposited NiTi Alloy by Addition of La$_2$O$_3$." *Additive Manufacturing* 33: 101150. https://doi.org/10.1016/j.addma.2020.101150.

Lu, H. Z., L. H. Liu, C. Yang, X. Luo, C. H. Song, Z. Wang, J. Wang, et al. 2022. "Simultaneous Enhancement of Mechanical and Shape Memory Properties by Heat-Treatment Homogenization of Ti$_2$Ni Precipitates in TiNi Shape Memory Alloy Fabricated by Selective Laser Melting." *Journal of Materials Science & Technology* 101: 205–216. https://doi.org/10.1016/j.jmst.2021.06.019.

Lu, H. Z., H. W. Ma, W. S. Cai, X. Luo, Z. Wang, C. H. Song, S. Yin, and C. Yang. 2021. "Stable Tensile Recovery Strain Induced by a Ni4Ti3 Nanoprecipitate in a Ni50.4Ti49.6 Shape Memory Alloy Fabricated via Selective Laser Melting." *Acta Materialia* 219: 117261. https://doi.org/10.1016/j.actamat.2021.117261.

Lu, H. Z., C. Yang, X. Luo, H. W. Ma, B. Song, Y. Y. Li, and L. C. Zhang. 2019. "Ultrahigh-performance TiNi Shape Memory Alloy by 4D Printing." *Materials Science and Engineering: A* 763: 138166. https://doi.org/10.1016/j.msea.2019.138166.

Luo, X., L. H. Liu, C. Yang, H. Z. Lu, H. W. Ma, Z. Wang, D. D. Li, L. C. Zhang, and Y. Y. Li. 2021. "Overcoming the Strength–Ductility Trade-off by Tailoring Grain-Boundary Metastable Si-Containing Phase in β-Type Titanium Alloy." *Journal of Materials Science & Technology* 68: 112–123. https://doi.org/10.1016/j.jmst.2020.06.053.

Martin, J. H., B. D. Yahata, J. M. Hundley, J. A. Mayer, T. A. Schaedler, and T. M. Pollock. 2017. "3D Printing of High-Strength Aluminium Alloys." *Nature* 549 (7672): 365–369. https://doi.org/10.1038/nature23894.

Moghaddam, S. N., S. Saedi, A. Amerinatanzi, A. Hinojos, A. Ramazani, J. Kundin, M. J. Mills, H. Karaca, and M. Elahinia. 2019. "Achieving Superelasticity in Additively Manufactured NiTi in Compression Without Post-Process Heat Treatment." *Scientific Reports* 9 (1): 41. https://doi.org/10.1038/s41598-018-36641-4.

Nagarajan, R., and K. Chattopadhyay. 1994. "Intermetallic Ti$_2$Ni/TiNi Nanocomposite by Rapid Solidification." *Acta Metallurgica et Materialia* 42 (3): 947–958.

Oliveira, J. P., A. J. Cavaleiro, N. Schell, A. Stark, R. M. Miranda, J. L. Ocana, and F. M. Braz Fernandes. 2018. "Effects of Laser Processing on the Transformation Characteristics of NiTi: A Contribute to Additive Manufacturing." *Scripta Materialia* 152: 122–126. https://doi.org/10.1016/j.scriptamat.2018.04.024.

Oliveira, J. P., R. M. Miranda, and F. M. Braz Fernandes. 2017. "Welding and Joining of NiTi Shape Memory Alloys: A Review." *Progress in Materials Science* 88: 412–466. https://doi.org/10.1016/j.pmatsci.2017.04.008.

Otsuka, K., and X. Ren. 2005. "Physical Metallurgy of Ti–Ni-Based Shape Memory Alloys." *Progress in Materials Science*

50 (5): 511–678. https://doi.org/10.1016/j.pmatsci.2004.10.001.

Sam, J., B. Franco, J. Ma, I. Karaman, A. Elwany, and J. H. Mabe. 2018. "Tensile Actuation Response of Additively Manufactured Nickel-Titanium Shape Memory Alloys." *Scripta Materialia* 146: 164–168. https://doi.org/10.1016/j.scriptamat.2017.11.013.

Tomozawa, M., H. Y. Kim, and S. Miyazaki. 2009. "Shape Memory Behavior and Internal Structure of Ti–Ni–Cu Shape Memory Alloy Thin Films and Their Application for Microactuators." *Acta Materialia* 57 (2): 441–452. https://doi.org/10.1016/j.actamat.2008.09.026.

Toprek, D., J. Belosevic-Cavor, and V. Koteski. 2015. "Ab Initio Studies of the Structural, Elastic, Electronic and Thermal Properties of $NiTi_2$ Intermetallic." *Journal of Physics and Chemistry of Solids* 85: 197–205. https://doi.org/10.1016/j.jpcs.2015.05.019.

Verhaeghe, F., T. Craeghs, J. Heulens, and L. Pandelaers. 2009. "A Pragmatic Model for Selective Laser Melting with Evaporation." *Acta Materialia* 57 (20): 6006–6012. https://doi.org/10.1016/j.actamat.2009.08.027.

Wagner, Martin F. X., and W. Windl. 2009. "Elastic Anisotropy of Ni_4Ti_3 from First Principles." *Scripta Materialia* 60 (4): 207–210. https://doi.org/10.1016/j.scriptamat.2008.09.028.

Wang, X., S. Kustov, K. Li, D. Schryvers, B. Verlinden, and J. V. Humbeeck. 2015. "Effect of Nanoprecipitates on the Transformation Behavior and Functional Properties of a Ti–50.8 at.% Ni Alloy with Micron-Sized Grains." *Acta Materialia* 82: 224–233. https://doi.org/10.1016/j.actamat.2014.09.018

Yan, W., Y. Qian, W. Ma, B. Zhou, Y. Shen, and F. Lin. 2017. "Modeling and Experimental Validation of the Electron Beam Selective Melting Process." *Engineering* 3 (5): 701–707. https://doi.org/10.1016/j.eng.2017.05.021.

Zhang, B., J. Chen, and C. Coddet. 2013. "Microstructure and Transformation Behavior of in-situ Shape Memory Alloys by Selective Laser Melting Ti–Ni Mixed Powder." *Journal of Materials Science & Technology* 29 (9): 863–867. https://doi.org/10.1016/j.jmst.2013.05.006.

Zhang, T., and C. Liu. 2022. "Design of titanium alloys by additive manufacturing: A critical review." *Advanced Powder Materials* 1: 100014. doi: 10.1016/j.apmate.2021.11.001.

Zhou, Q., M. D. Hayat, G. Chen, S. Cai, X. Qu, H. Tang, and P. Cao. 2019. "Selective Electron Beam Melting of NiTi: Microstructure, Phase Transformation and Mechanical Properties." *Materials Science and Engineering: A* 744: 290–298. https://doi.org/10.1016/j.msea.2018.12.023.